Neuron, volume *60*

Supplemental Data

Tuning of Synaptic Integration in the Medial Entorhinal Cortex to the Organization of Grid Cell Firing Fields

Derek L.F. Garden, Paul D. Dodson, Cian O'Donnell, Melanie D. White, and Matthew F. Nolan

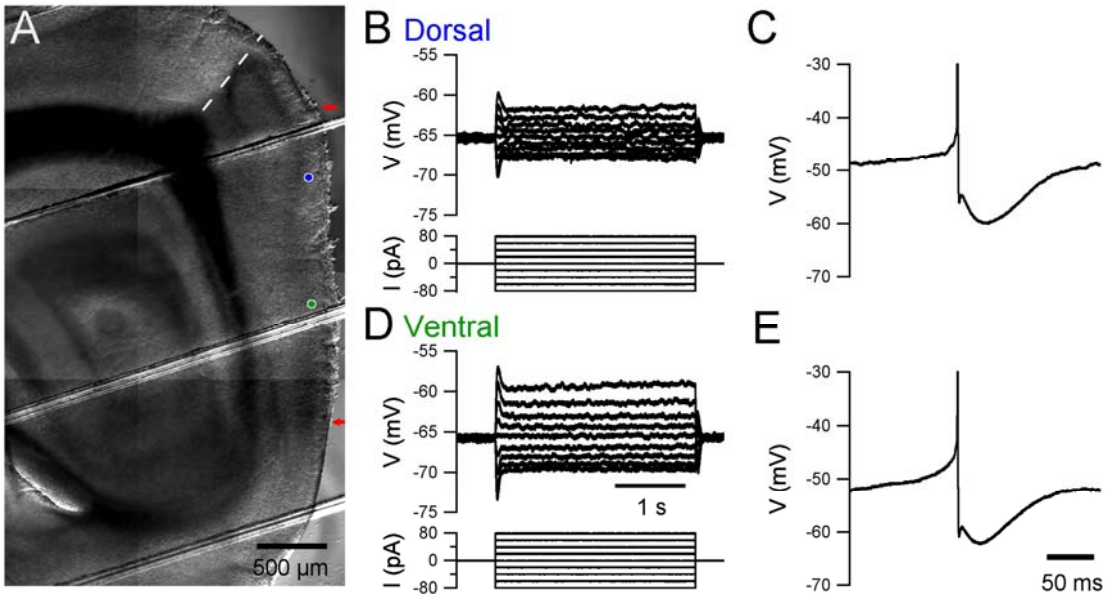

Supplemental Figure 1. Stellate cell location and membrane properties

(A) Parasagittal brain slice under the experimental microscope. The medial entorhinal cortex is on the right of the image. The border between the postrhinal cortex and sensory cortex is indicated by a dashed line, while the dorsal and ventral borders of the MEC are indicated by red arrows. The position of the dorsal cell in parts B and C, located 506 µm from the dorsal MEC border, and the ventral cell in parts D and E, located 1530 µm from the dorsal MEC border, are shown on this representative section as blue and green circles respectively.

(B and D) Examples of membrane potential responses (upper traces) to current steps (lower traces) recorded from a dorsal stellate neuron (B) and a ventral stellate neuron (D).

(C and E) Examples of afterhyperpolarizations (AHPs) following action potentials recorded from the dorsal neuron (C) and the ventral neuron (E). The more hyperpolarized membrane potential reached during the peak of the slow AHP compared with the peak of the fast AHP is typical of stellate neurons. Both action potentials are in response to threshold current steps of duration three seconds, and amplitude 260 pA for the dorsal neuron (C) and 130 pA for the ventral neuron (E). The action potentials in both panels are truncated.

The parasagittal brain slices were prepared as follows. Mice were decapitated, their brains rapidly removed and placed in cold (4°C) modified ACSF of composition (mM): NaCl (86), NaH_2PO_4 (1.2), KCl (2.5), $NaHCO_3$ (25), Glucose (25), $CaCl_2$ (0.5), $MgCl_2$ (7), sucrose (75). The brain was hemisected, glued medial surface down to the stage of a Vibratome 3000 sectioning system and cut submerged under cold modified ACSF into 400 µm sagittal sections. Slices were transferred to a storage container filled with standard ACSF at 33-35°C for 10 - 20 mins and cooled to room temperature (20-24°C).

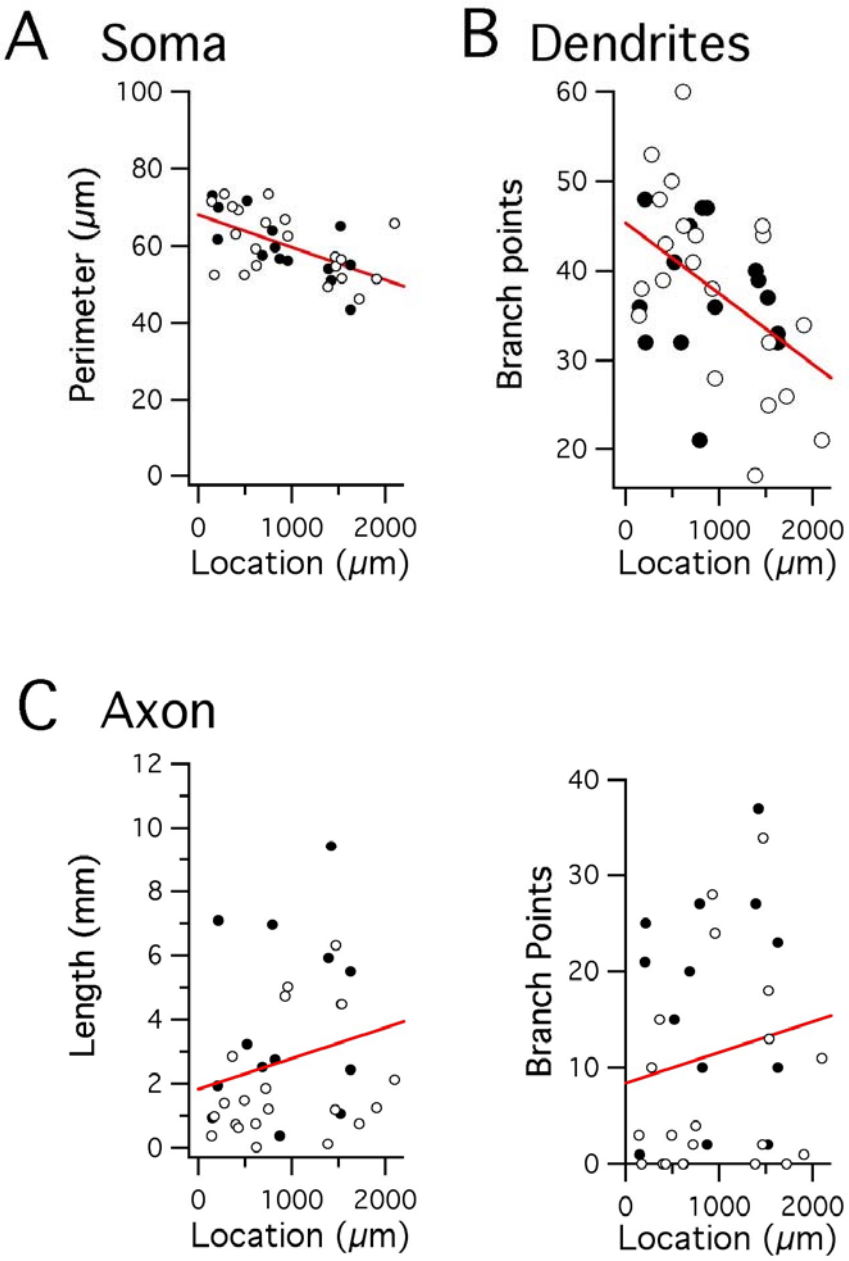

Supplemental Figure 2. Additional morphological properties of stellate neurons.

(A) The perimeter of reconstructed stellate cells plotted as a function of the location of their soma along the dorsal-ventral axis of the entorhinal cortex.
(B) The number of dendritic branch for the reconstructed stellate cells plotted as a function of soma location.
(C) The number of branch points (top) and the total length (bottom) for the axons of reconstructed stellate cells plotted as a function of soma location. Some axons did not appear to branch, whereas others had numerous local collaterals, but there was no apparent organization along the dorsal-ventral axis.

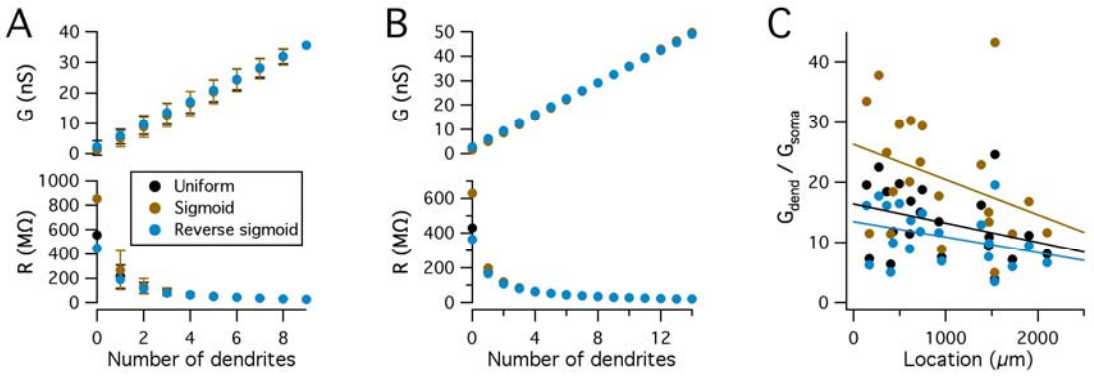

Supplemental Figure 3. Relationship between the number of primary dendrites and the somatically recorded membrane properties of stellate neurons
The primary dendrites were systematically removed from each of the model neurons in Figure 5 and the somatic input resistance measured for all possible combinations of primary dendrites. All neurons contain a passive membrane conductance with density adjusted to match the experimentally recorded input resistance when all dendrites are present (see Figure 5).
(A) Input conductance (top) and input resistance (bottom) plotted as a function of the number of dendrites for a representative stellate neuron that had 9 primary dendrites. Separate estimates were made for the assumptions of a uniformly distributed membrane conductance as well as sigmoid and reverse sigmoid distributions.
(B) Input conductance (top) and input resistance (bottom) plotted as a function of the number of dendrites for an idealized neuron with somatic input conductance determined from the mean input conductance of the isolated soma of all 21 reconstructed neurons and the dendritic conductance determined from the mean contribution to the somatically measured input conductance of each dendrite from each of the 21 reconstructed neurons. Separate estimates were made for the assumptions of a uniformly distributed membrane conductance as well as sigmoid and reverse sigmoid distributions.
(C) Ratio of the somatic input conductance to the total dendritic conductance measured from the soma plotted as a function of location of each reconstructed stellate neuron. While the more dorsal neurons have a larger soma (Figure 5), the dendrites nevertheless dominate the somatically measured input resistance. The relationship between the soma to dendrite conductance ratio and location is not significant ($p > 0.1$) for the uniform, sigmoid or reverse sigmoid cases.

Detailed procedures for the simulations in this and other figures were as follows. Simulations were performed using the NEURON simulation environment, version 5.9 or 6.0 (Carnevale and Hines, 2006). Cell morphologies were converted from Neurolucida files to NEURON geometry files using the Import3D function in NEURON. The membrane capacitance, C_m was set to 1 μFcm^{-2} and the axial resistivity, R_i set to 100 Ωcm. The time step for all simulations was set to 0.025 ms.

For passive models in Figure 5H, a passive membrane conductance with a reversal potential of -70mV was applied to the soma and dendrites following several different sub-cellular distribution rules. 1) The same membrane conductance of 0.0001 S cm^{-2} distributed uniformly throughout the soma and dendrites of each model cell (uniform density); 2) a constant total membrane conductance of 25 nS per cell, regardless of the neuron's size (uniform total); 3) a sigmoid increase in conductance with distance from the cell body (sigmoid); 4) a sigmoid decrease in conductance with distance from the cell body (reverse sigmoid).

For the sigmoid distribution (Stuart and Spruston, 1998), the membrane conductance density of each section of the cell, g_m, was set according to

$$g_m = g_{soma} + \frac{4g_{soma}}{1 + e^{(d_{half} - dis)/steep}}$$

where g_{soma} is the conductance density at the soma, d_{half} is the distance at which the function is halfway between g_{soma} and g_m's maximum, *dis* is the dendritic distance from the soma and *steep* determines the steepness of the increase with distance. Setting d_{half} to 200 μm and *steep* to 50 μm provided a membrane conductance density at the distal dendrites which is five times the somatic conductance density. In all cases g_{soma} was scaled so that the cell's total conductance equalled the case where a uniform conductance of 0.0001 S cm^{-2} was applied. All axons had a passive leak conductance of 2e-5 S cm^{-2} with a reversal potential of -70 mV.

For versions of the models that contained I_h, the membrane conductance density at the resting membrane potential of -70 mV was identical to the corresponding passive models. The three conductances used were a passive leak potassium conductance with reversal potential -105 mV, a passive leak sodium conductance with reversal potential +40 mV and an I_h conductance with reversal potential -40 mV. A simplified two-state model of I_h that appoximates currents measured with voltage-clamp experiments was used for the simulations (Nolan et al., 2007). The rate constants for transitions between open and closed states were, rate = A/(1+ exp(-k*(d-v))), where A = 0.0366 ms^{-1}, k = 0.04 mV^{-1} and d = -118.75 for the open to closed transition, and A = 0.066 ms^{-1}, k = -0.09 mV^{-1} and d = -56.05 for the closed to open transition. In all model neurons the densites of the three conductances at -70 mV was fixed in a constant ratio of 0.4827:0.0173:0.5 (leak potassium: leak sodium: I_h). This ratio was chosen to account for the resting membrane potential and the change in input resistance caused by block of I_h, but qualitatively similar effects on synaptic integration are produced by a range of parameters, providing the total membrane conductance density at the resting membrane potential is equal to the value required to account for the experimentally measured input resistance (Figure 5H-I).

Synaptic inputs were added to the model using the Exp2Syn function built into NEURON, with time constants of 0.14 and 1.2 ms and a reversal potential of 0 mV. To evaluate EPSP waveforms, synapses were placed on all segments of the dendritic tree, the somatic response to a single stimulus at each location was recorded and the average reponse calculated for each neuron. The synaptic conductance weight was 1.8 nS and in all neurons the amplitude of the mean synaptic response was < 1 mV.

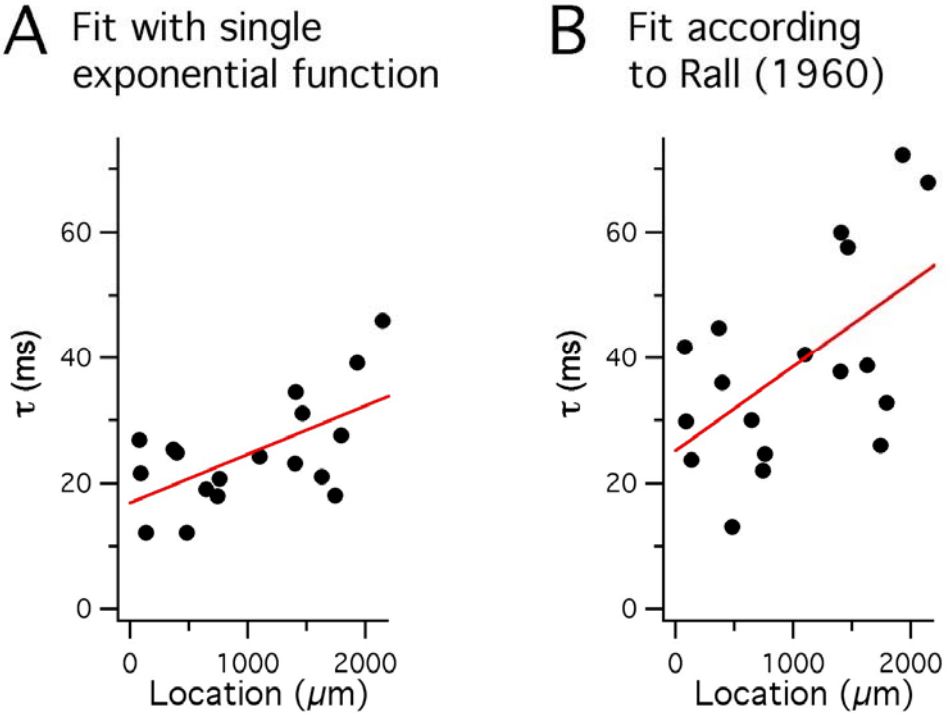

Supplemental Figure 4. Stellate neuron membrane time-constant varies as a function of dorsal-ventral location

(A) Time constants estimated by fitting membrane potential response to a current step with a single exponential function are plotted as a function of neuronal location along the dorsal-ventral axis of the MEC (slope = 7.7 ms μm^{-1}, R^2 = 0.33, p = 0.0078). All recordings were made in the presence of 10 µM ZD7288 to block I_h, together with 5 µM NBQX, 50 µM D-APV and 50 µM picrotoxin to block ionotropic glutamate and GABA receptors.

(B) Estimates of the membrane time constant that take account of current flow from the soma to the dendrites during the membrane potential response to a current step, are plotted as a function of neuronal location along the dorsal-ventral axis of the MEC (slope = 13.5 ms μm^{-1}, R^2 = 0.28, p = 0.015). The value of log{sqrt(t)(dV/dt)}, where V = membrane potential and t = time, was calculated at 5 – 10 ms intervals from the onset of the membrane potential response until the time at which the response reaches 95 % of its maximum value (Rall, 1960). The membrane time constant was then obtained from the inverse of the negative slope of a straight line fit to a plot of log{sqrt(t)(dV/dt)} as a function of time. Both (A) and (B) are for fits of the same data used to obtain input resistance measurements in the presence of ZD7277 (Figure 7A).

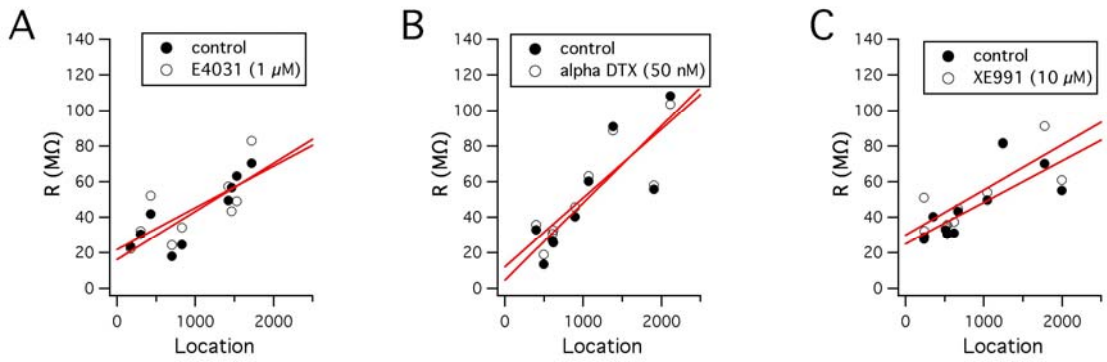

Supplemental Figure 5. Organization of the membrane properties of stellate cells in blockers of voltage-gated potassium channels

(A-C) Input resistance plotted as a function of location for stellate cells recorded in control conditions and then in the presence of E4031 to block ERG channels (R^2 = 0.67, p = 0.005; E4031, R^2 = 0.46, p = 0.03)(A), α-dendrotoxin to block Kv1 channels (control, R^2 = 0.68, p = 0.004; α-dendrotoxin, R^2 = 0.69, p = 0.003)(B) or XE9991 to block KCNQ channels (control, R^2 = 0.57, p = 0.004; E4031, R^2 = 0.56, p = 0.005)(C). The relative change in input resistance varied significantly as a function of location for α-dendrotoxin (p = 0.03), but not for E4031 (p = 0.46) or XE9991 (p = 0.58).

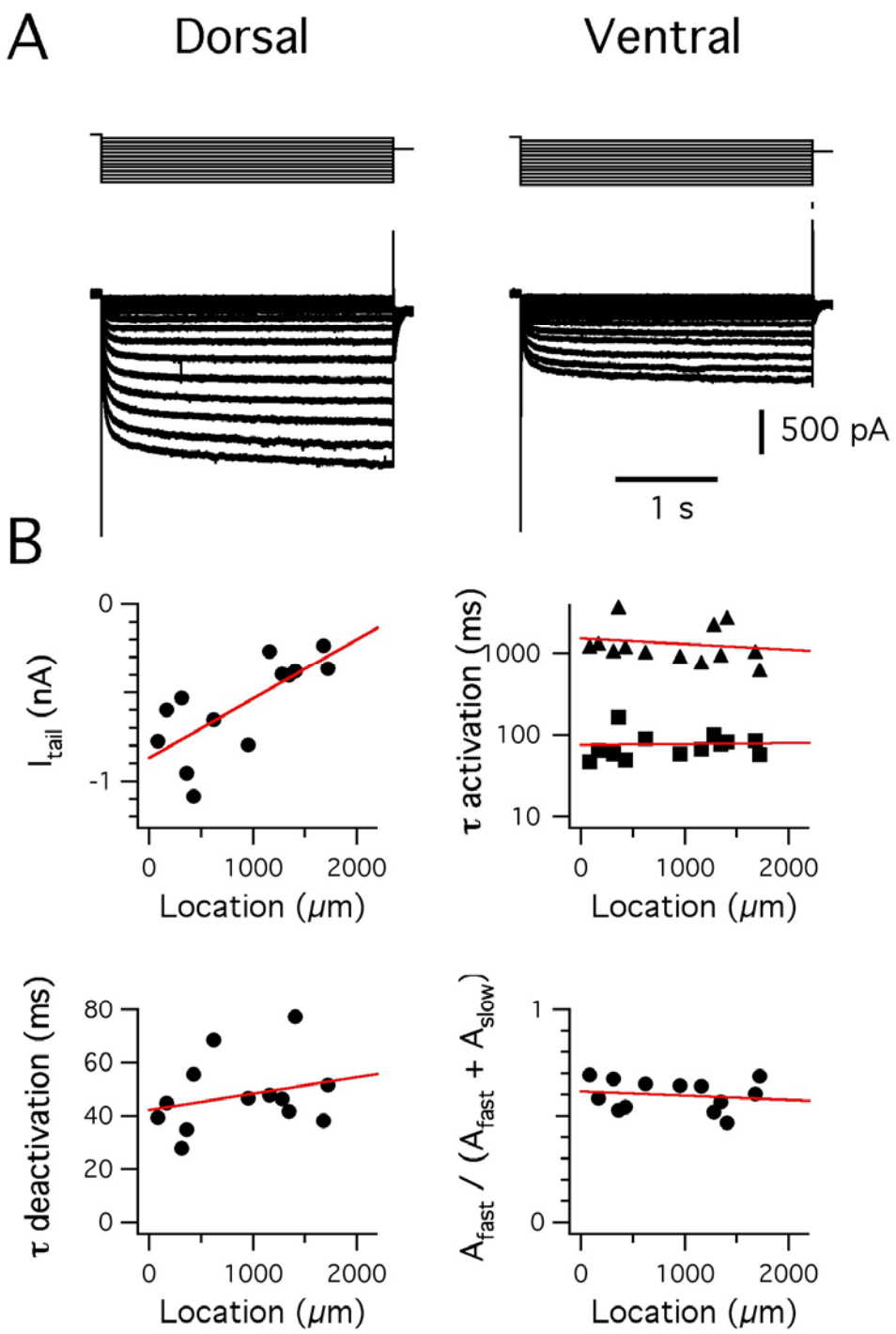

Supplemental Figure 6. The amplitude, but not the kinetics, of hyperpolarization-activated currents varies as a function of neuronal location

(A) Examples of membrane currents (lower traces) in response to a series of voltage-steps (upper traces) from a holding potential of -50 mV. The dorsal neuron is 80 µm and the ventral neuron 1157 µm from the dorsal border of the MEC.

(B) Tail current amplitude (upper left), fast and slow activation time constants for a step to -110 mV (upper right, fast activation time constant indicated by squares, slow activation time constant indicated by triangles), deactivation time constant (lower left) and relative amplitude of the fast time constant (lower right) are plotted as a function of location along the dorsal-ventral axis of the MEC. The tail current amplitude varies significantly as a function of position (slope = 334.4 pA μm^{-1}, $R^2 = 0.49$, p = 0.0044), but other properties of the hyperpolarization-activated current are independent of location (τ slow, p = 0.64; τ fast, p = 0.93; τ deact, p = 0.37; τ amplitude ratio, p = 0.59). We also did not find any evidence for differences in the voltage dependence of activation of hyperpolarization-activated currents (V_{half}, p = 0.663; slope, p = 0.104). Experimental procedures and analysis routines are as described in Nolan et al., 2007. All recordings were made in the presence of a cocktail of receptor antagonists and ion channel blockers designed to minimize the impact of other membrane ion channels on the measured currents.

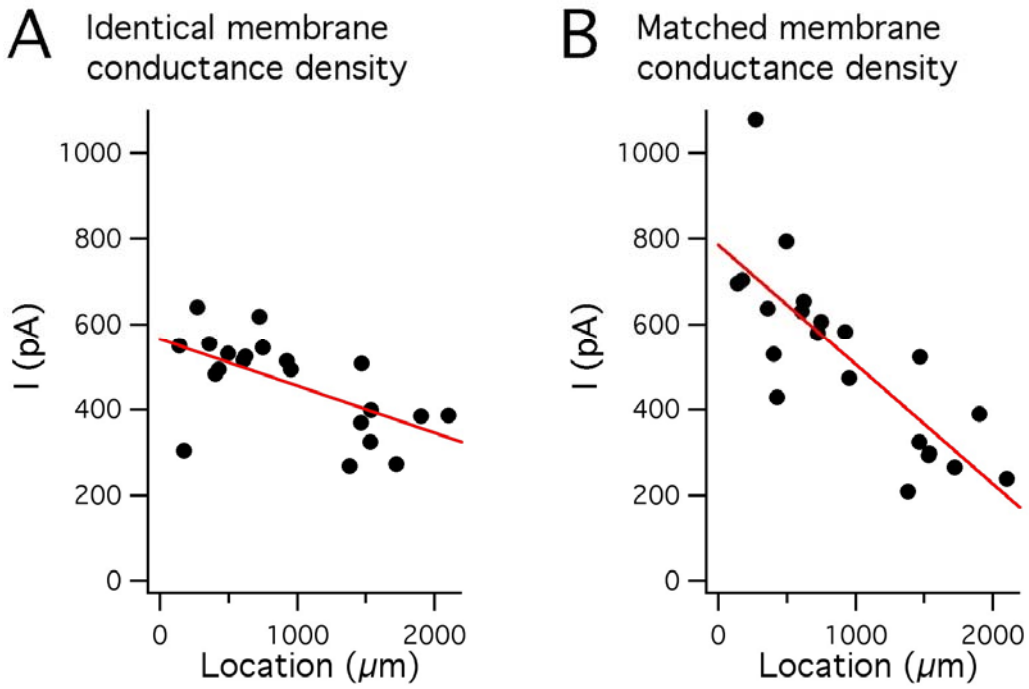

Supplemental Figure 7. Voltage-clamp measurements distinguish organization of membrane conductances by dorsal-ventral location

Since differences between the morphology of neurons with identical membrane conductance densities can in principle result in different somatically measured membrane currents, we sought to determine if somatic voltage-clamp recordings from stellate neurons can distinguish membrane conductances with densities that do vary as a function of dorsal-ventral location from those that do not. We carried out simulations of reconstructed neurons using the models in Figure 5. These simulations show that when all neurons contain an identical membrane conductance density, then the currents recorded from the most ventral neurons are expected to be 57.4 % of the corresponding currents from the most dorsal neurons (A). By contrast, when the membrane conductance density

is adjusted to account for the dorsal-ventral gradient in input resistance, then currents recorded from the most ventral neurons are expected to be only 21.8 % of the currents recorded from the most dorsal neurons (B). Thus, while differences in neuronal morphology lead to a shallow dorsal-ventral gradient in the simulated voltage-clamp current (A), this can be clearly distinguished from the substantially steeper dorsal-ventral gradient in the simulated voltage-clamp current that arises when the membrane conductance densities account for the experimentally measured input resistance (p = 0.0064)(B).

(A) The amplitude of current responses to 20 mV voltage steps are plotted as a function of location for simulations of neurons that each contain a passive membrane conductance with a density that is independent of location (slope = -109 pA mm^{-1}, R^2 = 0.34, p = 0.0035). The parameters of the model neurons are identical to the 'uniform density' condition in Figure 5B and therefore differences in the simulated voltage-clamp current are a result of differences in neuronal morphology.

(B) Current responses plotted as a function of location as in (A) except that the density of the membrane conductance is adjusted to reproduce the experimentally measured input resistance (slope -280 pA mm^{-1}, R^2 = 0.61, p = 1.7e-05). The parameters of the model neurons are identical to the models in Figure 5H and I. ANOVA indicated that the location-dependence of the measured current differed significantly between the conditions in (A) and (B) (condition, p = 0.0018; location, p = 6.3e-8; interaction between location and condition, p = 0.00164). The simulations included a recording electrode with series resistance of 5 MΩ, equivalent to the maximum uncompensated series resistance in our experimental conditions. Qualitatively similar results were also obtained with a series resistance of 15 MΩ.

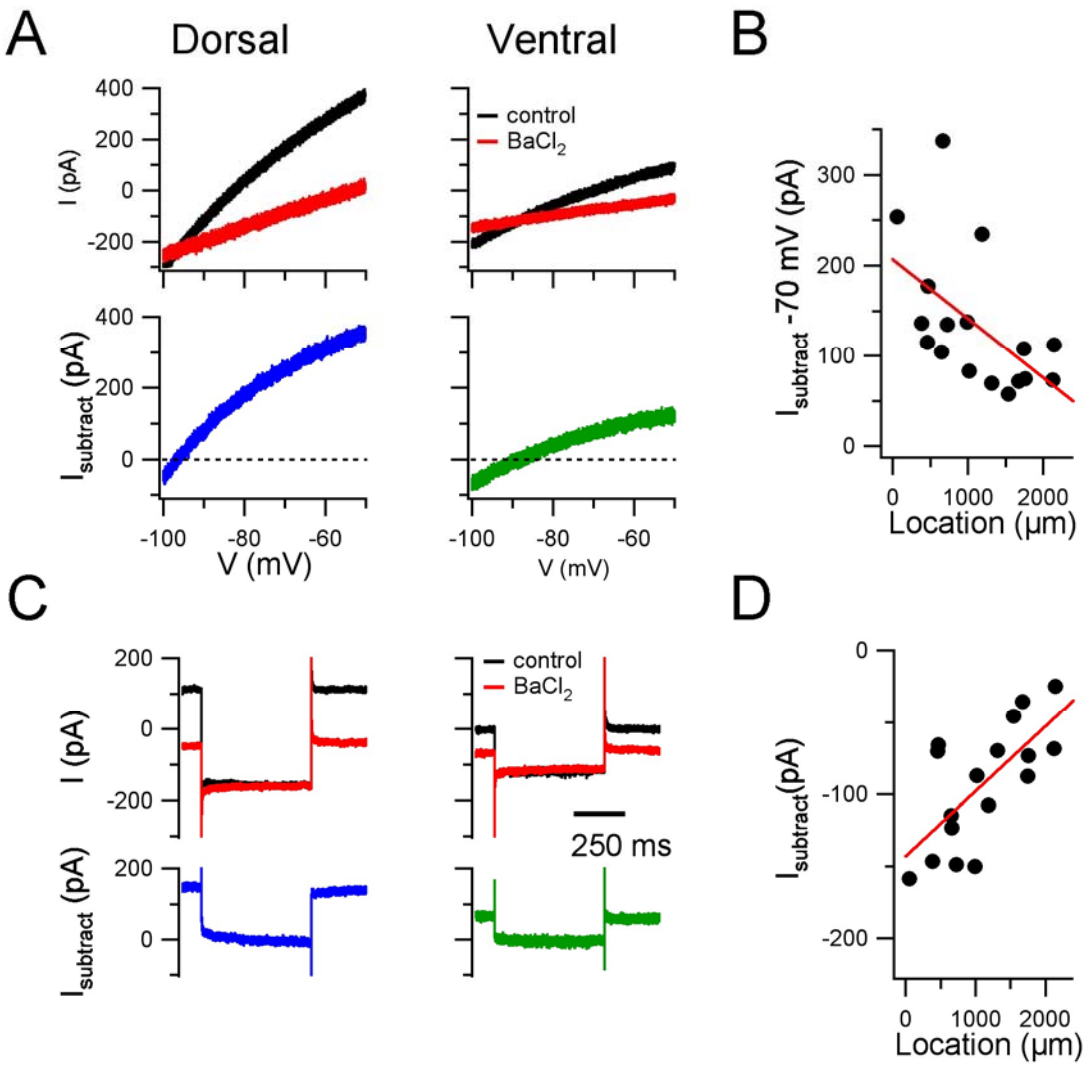

Supplemental Figure 8. The amplitude of a $BaCl_2$-sensitive potassium current varies as a function of dorsal-ventral location

(A) Membrane current plotted as a function of voltage for response to ramp-like changes in membrane potential. Current responses (upper plots) are recorded from a dorsal neuron (54 µm from the dorsal border of the MEC)(left column) and a ventral neuron (1756 µm from the dorsal border of the MEC) (right column) in control conditions and in the presence of $BaCl_2$. The $BaCl_2$-sensitive current (lower plots) is estimated by subtraction of the current in $BaCl_2$ from the control current.

(B) Amplitude of the $BaCl_2$-sensitive current at a membrane potential of -70 mV is plotted as a function of location (gradient = -65.7 pA μm^{-1}, $R^2 = 0.25$, $p = 0.023$).

(C) Membrane current responses (middle traces) to step changes in membrane potential (lower traces) recorded in control conditions and in the presence of $BaCl_2$. The $BaCl_2$ sensitive current (lower plots) is estimated by subtraction of the current in $BaCl_2$ from the control current.

(D) Amplitude of the $BaCl_2$-sensitive current plotted as a function of location (gradient = 45.1 pA μm^{-1}, $R^2 = 0.44$, $p = 0.0023$).

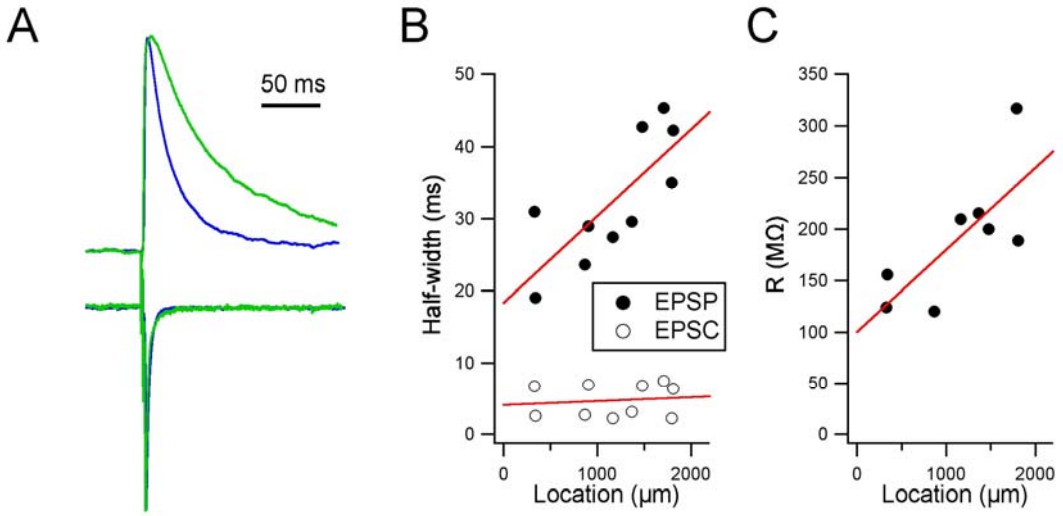

Supplemental Figure 9. The dorsal-ventral organization of synaptic integration is maintained after block of I_h with intracellular ZD7288

(A) Examples of normalized EPSPs (top) and EPSCs (bottom) recorded from dorsal (blue) and ventral (green) stellate neurons with I_h and voltage-gated Na^+ channels blocked by inclusion of 500 µM ZD7288 and 1 mM QX-314 in the intracellular solution. The dorsal neuron was located 339 µm and the ventral neuron 1792 µm from the dorsal border of the MEC.

(B) The half-widths of EPSPs (closed circles) and EPSCs (open circles) recorded with ZD7288 and QX-314 in the intracellular solution are plotted as a function of dorsal ventral location. Whereas the EPSP half-width varied steeply as a function of neuronal location (gradient = 0.54 ms mm-1, R2 = 0.54, p = 0.01), the EPSC half-width did not depend on location (gradient = 12.0 ms mm-1, R2 = -0.11, p = 0.72). ANOVA indicated significant differences between the half-widths of EPSPs and EPSCs (p = 0.01), between half-width at different locations (p = 0.00041) and differential dependence of the effect of location on the half-widths of EPSPs and EPSCs (p = 0.0086).

(C) Input resistance of the neurons in (B) plotted as a function of dorsal-ventral location (gradient = 79.4 MΩ mm^{-1}, R^2 = 0.47, p = 0.035).

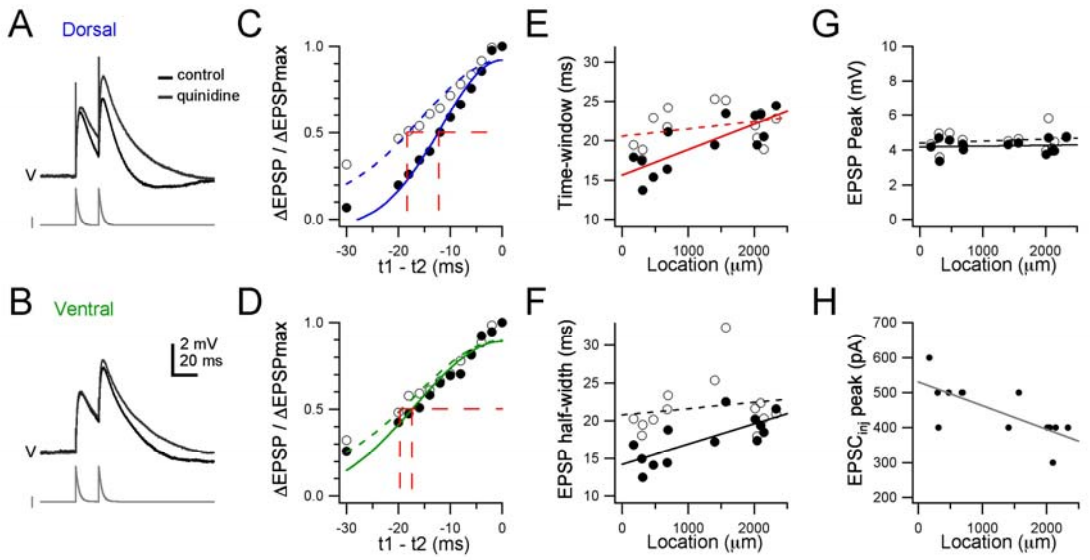

Supplemental Figure 10. Sensitivity of the time-window for integration of simulated synaptic inputs to quinidine

(A-B) Examples from a dorsal neuron (A) and a ventral neuron (B) of membrane potential responses (top) to pairs of injected EPSC-like current waveforms (bottom) in control conditions and during addition of 200 μM quinidine to the ACSF. In these traces the inter-stimulus interval is 20 ms. The neurons in (A) and (B) were located 679 μm and 2099 μm respectively from the dorsal border of the MEC. Simulated EPSPs were generated by injecting dual-exponential EPSC-like waveforms, with a rise-time of 0.2 ms and a decay time of 2.5 ms. The amplitude of the injected EPSC-like waveform was adjusted to evoke responses with a peak of approximately 4mV.

(C-D) The normalized peak depolarization of the second of a pair of EPSPs is plotted as a function of the interval between the injected EPSC-like waveforms for the corresponding neurons in (A-B).

(E) Estimates of the duration of the integration time-window plotted as a function of the location of each recorded neuron. In control conditions the time-window varies according to location ($R^2 = 0.62$, $p = 0.0009$), whereas in the presence of 200 μM quinidine there is no effect of location ($R^2 = -0.009$, $p = 0.36$).

(F) The half-width of EPSPs evoked by injection of simulated EPSCs is plotted as a function of location. In control conditions the half-width varies according to location ($R^2 = 0.52$, $p = 0.003$), whereas in the presence of 200 μM quinidine there is no effect of location (R2 = -0.06, p = 0.56).

(G-H) The peak depolarization relative to the resting membrane potential (G) and the corresponding maximum amplitude of the injected current waveform (H) used to evoke the simulated EPSPs are plotted as a function of location.

In (C-G) closed circles are data obtained in control conditions and open circles are data obtained in the presence of quinidine.

	MEC expression level
Sodium Channels	
NaV1.1 / Scn1a	+
NaV1.2 / Scn2a1	nd
NaV1.3 / Scn3a	-
NaV1.4 / Scn4a	+
NaV1.5 / Scn5a	-
NaV1.6 / Scn8a	++
NaV1.7 / Scn9a	-
NaV1.8 / Scn10a	+
NaV1.9	nd
Scn11a	+++
Scn2b	++
Scn1b	+++
Scn4b	+
Scn3b	+
Scn7a	-
Calcium Channels	
CaV1.1 / Cacna1s	-
CaV1.2 / Cacna1c	-
CaV1.3 / Cacna1d	++
CaV1.4 / Cacna1f	+
CaV2.1 / Cacna1a	+++
CaV2.2 / Cacna1b	+
CaV2.3 / Cacna1e	++
CaV3.1 / Cacna1g	++
CaV3.2 / Cacna1h	++
CaV3.3 / Cacna1i	++
Calcium Activated Potassium Channels	
KCa1.1 / Kcnma1	++
Kca2.1 / Kcnn1	-
KCa2.2 / Kcnn2	+
KCa2.3 / Kcnn3	++
KCa3.1 / Kcnn4	++
KCa4.1 / Kcnt1	-
KCa4.2 / Kcnt2	nd
KCa5.1 / Kcnu1	-
Voltage-gated Potassium Channels	
Kv1.1 / KCNA1	++
KCNAB1	++
KCNAB2	+
KCNAB3	++
Kv1.2 / KCNA2	+++

Kv1.3 / KCNA3	+
Kv1.4 / KCNA4	++
Kv1.5 / KCNA5	-
Kv1.6 / KCNA6	-
Kv1.7 / KCNA7	-
Kv1.8 / KCNA10	-
Kv2.1 / KCNB1	++
Kv2.2 / KCNB2	+
Kv3.1 / KCNC1	++
Kv3.2 / KCNC2	++
Kv3.3 / KCNC3	++
Kv3.4 / KCNC4	+
Kv4.1 / KCND1	-
Kv4.2 / KCND2	++
Kv4.3 / KCND3	-
Kv4.4 / KCND4	nd
Kv5.1 / KCNF1	+++
Kv6.1 / KCNG1	nd
Kv6.2 / KCNG2	nd
Kv6.3 / KCNG3	+
Kv6.4 / KCNG4	-
Kv7.1 / KCNQ1	-
Kv7.2 / KCNQ2	++
Kv7.3 / KCNQ3	++
Kv7.4 / KCNQ4	-
Kv7.5 / KCNQ5	++
Kv8.1 / KCNV1	++
Kv8.2 / KCNV2	++
Kv9.1 / KCNS1	nd
Kv9.2 / KCNS2	+
Kv9.3 / KCNS3	++
Kv10.1 / KCNH1	++
Kv10.2 / KCNH5	-
Kv11.1 / KCNH2	-
Kv11.2 / KCNH6	-
Kv11.3 / KCNH7	++
Kv12.1 / KCNH8	-
Kv12.2 / KCNH3	-
Kv12.3 / KCNH4	nd
Inwardly Rectifying Potassium Channels	
Kir1.1 / KCNJ1	nd
Kir2.1 / KCNJ2	-
Kir2.2 / KCNJ12	-
Kir2.3 / KCNJ4	+++
Kir2.4 / KCNJ14	-
Kir3.1 / KCNJ3	+++
Kir3.2 / KCNJ6	+
Kir3.3 / KCNJ9	+++

Kir3.4 / KCNJ5	-
Kir4.1 / KCNJ10	++
Kir4.2 / KCNJ15	-
Kir5.1 / KCNJ16	-
Kir6.1 / KCNJ8	-
Kir6.2 / KCNJ11	++
Kir7.1 / KCNJ13	nd
Two Pore Potassium Channels	
K2P1.1 / KCNK1	++
K2P2.1 / KCNK2	++
K2P3.1 / KCNK3	nd
K2P4.1 /KCNK4	-
K2P5.1 / KCNK5	-
K2P6.1 / KCNK6	-
K2P7.1 / KCNK7	-
K2P9.1 / KCNK9	+
K2P10.1 / KCNK10	++
K2P12.1 / KCNK12	nd
K2P13.1 / KCNK13	++
K2P15.1 / KCNK15	-
K2P16.1 / KCNK16	+
K2P17.1 / KCNK17	nd
K2P18.1 / KCNK18	++
HCN channels	
HCN1	++
HCN2	++
HCN3	-
HCN4	++
Housekeeping Genes	
GAPDPH	+++
Actb (beta actin)	+++
Actg1 (gamma actin cytoplasmic 1)	+++
Tuba1 (alpha 1 tubulin)	+++
Tubb2a (beta 2a tubulin)	+++

Supplemental Table 1.

Relative expression of ion channel mRNA in layer II of the MEC. Estimates of channel expression are obtained from data provided by the Allen Brain Atlas.

References

Carnevale, N.T., and Hines, M.L. (2006). The NEURON book (Cambridge, Cambridge University Press).

Nolan, M.F., Dudman, J.T., Dodson, P.D., and Santoro, B. (2007). HCN1 channels control resting and active integrative properties of stellate cells from layer II of the entorhinal cortex. J Neurosci *27*, 12440-12451.

Rall, W. (1960). Membrane potential transients and membrane time constant of motoneurons. Experimental neurology *2*, 503-532.

Stuart, G., and Spruston, N. (1998). Determinants of voltage attenuation in neocortical pyramidal neuron dendrites. J Neurosci *18*, 3501-3510.